Materials Advances

ROYAL SOCIETY OF CHEMISTRY

PAPER

View Article Online
View Journal | View Issue

Check for updates

Cite this: *Mater. Adv.*, 2022, 3, 7606

Mesoporous zinc platinate and platinum nanotubes: insights into the formation mechanism and their catalytic activity†

Shwetha Shetty,[a] Ankita Mathur,[b] Neha Sakhuja,[c] Dipanwita Chatterjee,[a] Subhajit Kundu,[a] Aditi Halder,[d] Navakanta Bhat[c] and N. Ravishankar*[a]

Received 26th January 2022,
Accepted 30th July 2022

DOI: 10.1039/d2ma00090c

rsc.li/materials-advances

Mesoporous nanostructures with their unique morphology, high accessible surface area, and numerous active sites have a distinct microstructural advantage over ultrafine nanoparticles. To incorporate hierarchical porosity, sacrificial template-based approaches are beneficial as they have the advantage of efficient rendering of morphology and simultaneous removal of the template material. It is also crucial to study the behavior of the template material and its reactivity with the deposited material under the reaction conditions. Herein, we have proposed an ultrafast microwave technique to synthesize mesoporous nanotubes of a novel phase zinc platinate (Zn_2PtO_4) using ZnO as a sacrificial template. We have observed that under the ultrafast kinetics offered by the microwave, aided with reaction temperature, the core ZnO reacts with the adhering hydrolyzed Pt precursor complex to form a mesoporous zinc platinate shell. By designing control experiments, we have attributed the mechanism of formation to a modified sacrificial template-assisted hydrolysis (STAH) process. The controlled, simple reduction step of Zn_2PtO_4 nanotubes using $NaBH_4$ results in the formation of mesoporous Pt nanotubes. The mesoporous nature of Zn_2PtO_4 nanotubes and enhanced surface area (54 m^2 g^{-1}) aids in highly sensitive (down to 300 ppb) and selective sulphur dioxide (SO_2) detection at room temperature. The mesoporous Pt nanotubes show exceptional catalytic activity towards the methanol oxidation reaction (MOR) and oxygen reduction reaction (ORR) which is attributed to their unique morphology. This synthesis strategy offers a unique approach to designing mesoporous structures of other zinc-based mixed metal oxides and conveniently converting them to their active metal counterparts.

1. Introduction

Nanotubes with porous shells and hollow cores are attractive as they exhibit superior electrical and thermal conductivities along with multiple interfaces (inner, outer, and pore walls) which are readily accessible for reactive molecules and guest species. Additional advantages such as low density, high surface area, and less usage of material make them find extensive use in diverse fields such as catalysis, sensing, energy storage, Surface-Enhanced Raman Spectroscopy (SERS), on-the-spot drug delivery, and enzyme encapsulation.[1–4] Engineering bimodal types of pores of sizes <2 nm (microporous) or 2–50 nm (mesoporous) having long hollow channels >50 nm (macroporous) hierarchically can give rise to novel functionality for materials.[5–8] Mesoporous materials have pore sizes adequate to host and immobilize large molecules like enzymes or DNA and are hence attractive in adsorption (or separation) and biosensing.[9–12] The presence of innumerable diffusion channels in these materials, which connect the surface to the bulk, enables extended reaction time leading to an enhanced response to chemical and electrical signals for the analyte molecules.[13]

Thermodynamically, introducing porosity in a crystalline solid is not feasible due to its inherent nature towards the formation of a close-packed structure.[14] In our earlier work, we have shown that reaction-limited aggregation can be a strategy to make mesoporous metal nanostructures.[15] The strategy is to limit the close packing order to nanoscopic dimensions and incorporate void spaces between them. Most of the synthesis methods involve pore directing agents in the form of short or long-chain polymers to create mesoporous structures of required pore dimensions.[16] Dealloying is another commonly

[a] *Materials Research Centre, Indian Institute of Science, 560012, Bangalore, India. E-mail: nravi@iisc.ac.in*
[b] *School of Engineering, IIT-Mandi, Kamand-175005, Himachal Pradesh, India*
[c] *Centre for Nanoscience and Engineering, Indian Institute of Science, 560012, Bangalore, India*
[d] *School of Basic Sciences, IIT-Mandi, Kamand-175005, Himachal Pradesh, India*

† Electronic supplementary information (ESI) available. See DOI: https://doi.org/10.1039/d2ma00090c

used technique where the selective dissolution of a chemically active metal from an alloy creates a self-supporting bicontinuous pore-ligament structure of the noble metal.[6,17–19] However, the dictating factors for porosity are the degree of alloying between the constituent metals and the surface diffusivity of the noble metal constituent, which determine the size of the pores and ligaments thereby limiting the versatility of this technique.[20,21] Literature shows that template-assisted methods are the best to form porous structures of a variety of materials.[5,22–25] Different methodologies are adopted for metal nucleation within the controlled and confined spaces provided by the hard or soft templates to form porous structures of a variety of materials with precise control over porosity and morphology.[5,26] The disadvantage is that the second step of template removal may be detrimental to the integrity of the porous structure and require harsher conditions.[27] A successful pore replication also depends on favorable interaction between the precursor material and the template, which requires that the surface properties of hard templates be modified.[28] Sacrificial templates and galvanic replacement strategies are handy in this regard as the whole process of introducing porosity and template removal happens simultaneously making the process simple, reproducible, and suitable for large-scale production.[29] Easily etchable metals such as silver, tellurium, nickel, and metal oxide supports such as zinc oxide or copper oxide are commonly used to synthesize porous noble metal nanostructures with guided morphologies.[30–39] However, the challenge here is that the reaction kinetics control the efficient pore formation and many times the template dissolution is time-consuming due to anisotropic etching.[40] Therefore, developing an ultrafast low-cost one-step scalable process for the synthesis of surfactant-free mesoporous nanostructures is promising.

Pt and Pt-based nanomaterials are widely used as commercial electrode materials in polymer electrolyte membrane fuel cells (PEMFCs) as it offers excellent hydrogen and alcohol oxidation capabilities along with superior selectivity towards the oxygen reduction reaction.[24] Pt alloyed with suitable oxophilic elements (such as Ru, Ni, Fe, Sn, *etc.*) shows better catalytic activity towards methanol oxidation due to the bifunctional mechanism, ligand, and geometric strain effects.[41–44] Introducing porosity in a catalyst imparts high surface area and contiguous ligaments that provide electron pathway channels together improving mass transport and interfacial reaction processes beneficial in catalysis and sensing.[28] In a PEMFC assembly, mesoporous Pt offers excellent mass-specific activity.[45] Mesoporous Pt is also attractive for biomedical applications due to the feasibility of imaging, photothermal effect, and drug loading/delivery capability.[46,47] Platinum oxide has excellent physicochemical properties and is a versatile catalyst due to the presence of oxygenated Pt, which evokes the bifunctional mechanism in effectively oxidizing the adsorbed CO species.[48–50] Oxidized Pt is also shown to be an excellent hydrogen sensor.[51] The hybrid PtO-ZnO shows enhanced catalytic and sensing properties as compared to ZnO due to the modification of the band structure.[52,53] There has been a consistent effort to synthesize mesoporous Pt nanostructures with tailored architecture over the years.[54,55] However, the reports on bulk scale synthesis of mesoporous Pt/Pt oxide-based nanostructures are limited. Novel compositions of mixed Pt oxide and ZnO can bring in a cost-effective strategy for materials development and for realizing novel functionalities and applications.

Sensor materials, which belong to the type of chemiresistors that are semiconductor metal oxides like ZnO, SnO_2, WO_3, and V_2O_5, have been used for the detection of several toxic gases like NH_3, SO_2, H_2S, and NO_2.[56] SO_2 is one of the noxious pollutants released from the petrochemical industry, power plants, metal smelting, food industry, and processing of wine and requires precise detection and monitoring.[57] These toxic emissions from industrial and anthropogenic sources are responsible for global warming, ozone depletion, and health hazards.[58] Though chemiresistors have attractive attributes like high sensitivity, thermal stability, and high shelf-life, they suffer from a drawback of high operating temperature. This is one of the important concerns with respect to power consumption, increase in circuit complexity, and cost due to the incorporation of micro heaters beneath the sensors. Moreover, the high-temperature operation may cause structure or morphology transformations in the sensing film over a period.[59] The need of the hour is to develop new materials that can detect SO_2 with high sensitivity and selectivity at room temperature.

Herein, we have proposed a simple, one-step, surfactant-free, microwave-induced aqueous phase scalable synthesis method to produce mesoporous zinc platinate (Zn_2PtO_4) nanotubes using high aspect ratio ZnO nanorods as sacrificial templates and controlled conversion of this novel phase into mesoporous Pt nanotubes. ZnO is a versatile template as it promotes the hydrolysis of metal precursors by self-dissolution resulting in the formation of hollow/porous structures on top of that ZnO can be synthesized in a variety of forms in 0D, 1D, and 3D, which helps in engineering the morphology of these porous structures.[60,61] Additionally, the microwave technique offers an ultrafast rapid synthesis route with efficient energy utilization, a cost-effective and industrially viable option for the bulk synthesis of porous structures.[62] The literature shows that extreme conditions of high oxygen partial pressure, high temperature, and prolonged reaction time are required for the synthesis of Zn_2PtO_4.[63,64] In our case, the weak reducing ability of water along with superior reaction kinetics provided by the microwave reaction results in the adsorption-induced mixing of $[PtCl_6]^-$ with dielectrically heated ZnO to form the zinc platinate phase. Based on control experiments we propose a modified sacrificial template accelerated hydrolysis (STAH) process wherein the template also reacts and participates in the formation of the shell material.[60,65–67] We have carried out detailed electron microscopy studies to understand the mechanism of formation of the phase and morphology. The absence of any size controlling organic ligands gives these porous nanotubes free surfaces suitable for catalytic applications. The high surface area, the oxidation state of Pt, and the hierarchical porosity with one-dimensional morphology of Zn_2PtO_4 motivated us to test the gas sensing capabilities of this material and we have shown that indeed Zn_2PtO_4 shows high sensitivity, selectivity,

and reproducibility towards SO_2 sensing at room temperature. The mesoporous Pt nanotubes show excellent electrochemical methanol oxidation capabilities, and the ORR activity is comparable to that of the commercial platinum catalyst.

2. Experimental

2.1 Synthesis of ZnO nanorods

ZnO nanorods are synthesized by the modified Pacholski method.[68,69] Zinc acetate (14.75 g, 0.76 M) is dissolved in methanol at 65 °C under vigorous stirring and a solution of potassium hydroxide (7.4 g, 4 M) in methanol is slowly added. The mixture is aged for 2 hours at 60 °C to evaporate about half the volume of the solvent. This concentrated solution is transferred to a 50 mL Teflon vessel and then sealed in a stainless-steel autoclave. This is heated to 120 °C for 8 hours. The white precipitate obtained is washed well with methanol and dried in an oven.

2.2 Synthesis of porous nanotubes

10 mg of the as-prepared ZnO nanotube powder is dispersed in Milli-Q water and sonicated for 2 min. To this, 12 mM hexachloroplatinic acid is added and stirred well for it to dissolve. The entire mixture is transferred to a microwave transparent vessel provided with the Discover-CEM S-class microwave oven. Microwave heating is carried out under closed vessel conditions with high stirring. The reaction temperature is set at 200 °C for 5 min. The microwave power is set at 150 W, which ensures a ramping time of 3 min. After the system is cooled, the vessel is taken out. The obtained yellow powder is separated from the solvent by centrifugation at 2000 rpm for 2 min. The pH of the supernatant is checked using a glass pH electrode which is previously calibrated using standard pH 4 and pH 7 solutions. The obtained yellow powder is washed well with water until the pH is neutral. The final wash is done with acetone and the powder is collected by centrifugation and vacuum dried. This sample is labeled as pZPO-NTs. It is then re-dispersed in 50 mL of Milli-Q water by magnetic stirring. To this, sodium borohydride solution (10 mg mL^{-1}) is added dropwise. The solution is stirred for another 30 min and centrifuged to separate the black powder, which is washed thoroughly with water and acetone, and dried in the oven. This sample is labeled as pPt-NTs (for detailed experimental methods and characterization techniques refer to the ESI†).

3. Results and discussion

ZnO is a versatile template to synthesize novel material nanostructures with hollow interiors due to the ease of etching of ZnO in an acidic medium or reducing atmosphere.[67,70–76] In our work, porous platinum nanotubes are synthesized by the microwave-induced reaction between chloroplatinic acid and ZnO nanorods in an aqueous medium. The dual role of ZnO nanorods as sacrificial templates and as morphology-directing agents guides the formation of porous nanotubes during the microwave reaction. To begin with, ZnO nanorods of the required aspect ratio are synthesized by the hydrothermal method. The length of the nanorods can be tuned by changing the incubation time during the hydrothermal synthesis.[77] X-Ray diffraction (XRD) and scanning electron microscopy (SEM) studies show that high-aspect-ratio phase-pure (hexagonal wurtzite, *P*63*mc*, ICDD-00-036-1451) nanorods are formed (Fig. S1, ESI†). The nanorods have a hexagonal prismatic morphology with diameters ranging from 20–90 nm and lengths of 0.5–2 μm.

The methodology for the synthesis of porous nanotubes using ZnO nanorods as sacrificial templates is shown in Fig. 1. ZnO nanorods, dispersed in an aqueous solution of platinum precursor (H_2PtCl_6), are subjected to microwave heating at 200 °C. The yellow product obtained is stable under ambient conditions and designated as pZPO-NTs. X-ray diffraction (XRD) studies (Fig. 2a) show the presence of 3 broad peaks with maxima at 18.4°, 34.8°, and 59.4°, respectively. The particle size is ~1.7 nm as calculated from the Scherrer formula considering the Gaussian width of the first peak. Broadening due to sub 2 nm particle size along with the absence of peaks corresponding to ZnO or Pt phases confirms the single phase, and the peaks can be indexed to the inverse spinel face-centered cubic Zn_2PtO_4 phase (ICDD 00-023-1499).[64] The STEM-HAADF image shows that the core ZnO is completely etched resulting in the formation of hollow porous tubes irrespective of the diameter or the length of the nanorods (Fig. 2b). Also, the newly formed shell is nearly uniform in thickness, in the range of 10–15 nm, and it is made up of tiny particles of size ~1–2 nm as confirmed from the bright field transmission electron microscopy (BF-TEM) of this sample (Fig. 1e). STEM-EDS elemental mapping (Fig. 2c) and the line scan from a single nanotube (inset in Fig. 2b) show the presence of all 3 elements Zn, Pt and O. X-ray photoelectron

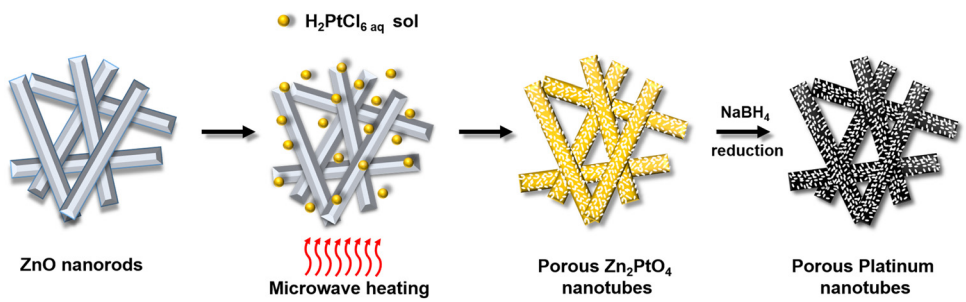

Fig. 1 Schematic of the formation of porous zinc platinate nanotubes and their conversion to porous platinum nanotubes.

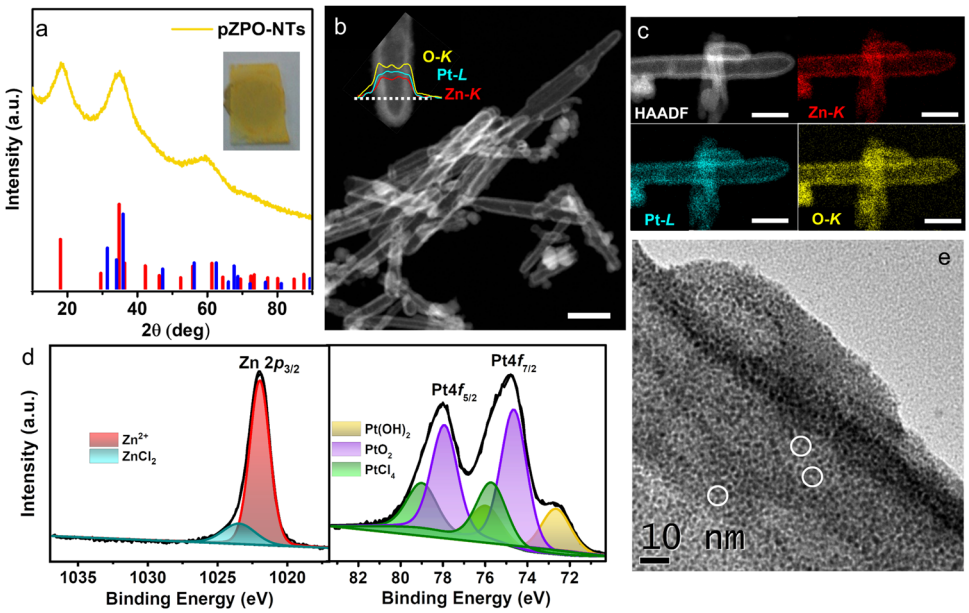

Fig. 2 (a) XRD pattern from as-synthesized porous zinc platinate nanotubes (pZPO-NTs) which can be matched to ICDD file 00-023-1499 for the standard zinc platinate phase (red line). The standard XRD pattern for the ZnO phase (ICDD-00-036-145) is shown in blue. The inset shows a photograph of the as prepared pZPO-NTs film on a glass substrate. (b) HAADF-STEM images of pZPO-NTs confirming the hollow interior and porous nature of the nanotubes. The inset shows the STEM-EDS line scan taken along the diameter of a nanotube for the Zn-*K*, Pt-*L*, and O-*K* lines. (c) STEM-EDS elemental mapping for Zn-*K*, Pt-*L* and O-*K*, respectively, taken from a single nanotube showing the distribution of the elements. (d) Core level elemental XPS scans from Zn 2p 3/2 and Pt 4f from the pZPO-NTs sample. Zn exists in +2 oxidation state and Pt exists in multiple oxidation states of +2 and +4. Traces of $ZnCl_2$ are found on the surface of the nanotubes. The precursor $PtCl_4$ signal is also seen in a trace amount on the surface of the sample. (e) High magnification BF-TEM image of a single pZPO-NT showing that the shell is composed of fine crystallites of size between 1–2 nm with a well-developed pore network. Pores are highlighted by white circles. The scale bar in (b) is 200 nm and (c) is 70 nm.

spectroscopy (XPS) studies of the as-synthesized pZPO-NTs are shown in Fig. 2d. Pt4f core level spectra from this sample show that platinum is in a higher oxidation state of +2 and +4. The binding energy values 72.6 eV, 74.6 eV, and 75.7 eV can be assigned to $Pt(OH)_2$, PtO_2, and $PtCl_4$, respectively, based on the standard NIST database.[51,78,79] The 72.6 eV doublet is also assigned to the PtO phase.[80] All Pt species are constrained to have a doublet separation of 3.3 eV and the FWHM is kept the same for 4f 7/2 and 4f 5/2 peaks of each pair. Even after the reaction, $PtCl_4$ may still be present in the precursor state adhered to the sample surface. The presence of $PtCl_4$ is always found in H_2PtCl_6 solution-impregnated solid oxide supports.[79] The Zn 2p signal mainly comes from Zn^{2+} species at a binding energy value of 1022.0 eV. A small shoulder peak at the higher binding energy side at 1023.4 eV is from $ZnCl_2$ species adhered to the surface of the porous pZPO-NTs.[81] From XPS data, a quantitative measurement of surface composition can also be done after background subtraction of the peak intensities and normalizing with respect to the relative sensitivity factor.[82] The relative sensitivity factor values for the elements Zn 2p, Pt 4f, and O 1s are 5.589, 5.575, and 0.71, respectively, as mentioned in the Kratos instrument database. The composition ratio measured from the normalized area under the peak for Zn 2p and Pt 4f is 2 : 1 for the Zn_2PtO_4 phase. The diffuse reflectance spectra for ZnO nanorods and pZPO-NTs are shown in Fig. S2a (ESI†). Pure ZnO is white in color and does not absorb in the visible range and has absorption maxima in the IR range; the absorption edge in the zinc platinate phase is red-shifted as compared to pure ZnO and seen at around 500 nm. The multiple absorption bands present in zinc platinate may be due to the presence of oxygen vacancies.[83,84] Since the particle size in the zinc platinate phase is between 1–2 nm, which exists in an inverse spinel structure with a large lattice parameter of ~8.5 Å, it is understandable that the structure may be non-stoichiometric and suffers from severe surface stresses. In spinel or inverse spinel materials, the presence of 2 or more different transition metal cations in different coordination environments (octahedral, tetrahedral, or mixed) can cause multiple LMCT (ligand to metal charge transfer) and IVCT (Intra valence charge transfer) transitions giving rise to multiple absorption bands in the visible and near IR region of the wavelength spectrum.[85,86] Tauc plots (Fig. S2b and c, ESI†) show a direct band gap of 3.2 eV for ZnO nanorods indicating the highly crystalline stoichiometric nature of the sample. pZPO-NTs show an indirect band gap of 1.8 eV. Due to the lack of data on the optical properties of the zinc platinate phase, reference to the Materials Project (MP, Lawrence Berkeley National Laboratory, Berkeley, CA) database is made which lists Zn_2PtO_4 as one of the metastable phases, and the calculated band gap value using LDA and GGA with a 50% underestimation is 0.8 eV.[87]

Zn_2PtO_4 is a rare phase and only a couple of papers exist in the literature which show the synthesis methodology. Muller and Roy have shown that by annealing a mixture of Zn $(OH)_2$ and platinum black at 900 °C under an oxygen partial pressure

of 200 atm for a prolonged duration (several days), light yellow-green colored Zn_2PtO_4 could be synthesized.[64] Kjelin and Palmqvist have synthesized nanoparticles of Zn_2PtO_4 by mixing $PtCl_4$ with ZnO in an Ar glovebox and annealing in a sealed quartz ampule under an N_2 atmosphere in a tube furnace.[63] Interestingly, a few research groups have also observed the formation of the zinc platinate phase at the interface between Pt and ZnO during non-equilibrium synthesis processes such as combustion synthesis, thin film growth, or aerosol condensation.[88–90] Microwave synthesis is known to offer ultra-fast reaction kinetics due to the rapid and uniform heating of the dielectric ZnO support and the reaction medium.[91] The pressure generated inside the microwave reaction vessel is ~250 psi (~15 atm) at the reaction temperature of 200 °C, which also aids the reaction kinetics.

To understand the mechanism of the formation of the zinc platinate phase, a set of control experiments is performed. To start with, the microwave reduction of the H_2PtCl_6 precursor is performed maintaining the exact conditions for the formation of pZPO-NTs in the absence of ZnO nanorods. No product is formed and the precursor solution remains clear but the color changes to deeper yellow (Fig. S3a, ESI†). The absence of any product formation shows that homogeneous nucleation of metallic Pt or PtO_2 is not possible under these reaction conditions. UV-Visible absorption spectroscopy of the solution before and after this control reaction displays peaks at 208 nm and 262 nm, which are assigned to ligand to metal charge transfer (LMCT) transitions of ligand σ and π orbitals of $PtCl_6^{2-}$ ions.[92] After the MW reaction, the solution turns deeper yellow with a decrease in pH from 3 to ~1 and the corresponding absorption spectra show lower intensity for both the peaks and a slightly elevated intensity in the 235 nm region suggesting the hydrolysis of H_2PtCl_6 into chloro-aquo complexes of the type $H_2[PtCl_nOH_{6-n}]$ due to the exchange of Cl^- with water. The released Cl^- ions into the solvent increase the acidity of the medium.[93,94] In the presence of ZnO nanorods, a clear supernatant and a yellow product are obtained after the microwave reaction (Fig. S3b, ESI†). The UV-Vis absorption spectra for the supernatant show no traces of $[PtCl_6]^{2-}$ ions suggesting a complete removal of the platinum precursor. The pH of the supernatant is ~5 at this stage, suggesting that the dissolution of ZnO nanorods increases the basicity of the medium. Even a prolonged microwave reaction period of 1 hour yields only the zinc platinate phase and not the Pt phase. The nanotubes are porous as earlier, but the shells are slightly thicker than that formed from the 5 min reaction. The shell thickness is in the range of 17–23 nm. The BF-TEM images for the porous pZPO-NTs nanotubes are shown in Fig. S4a and b (ESI†). The formation of the phase is confirmed by XRD (Fig. S4c, ESI†). This suggests that under microwave synthesis conditions, only zinc platinate is the stable phase formed and not Pt.

To check the effect of pH on the synthesis, the dried powder of pZPO-NTs is then re-dispersed in an aqueous medium and subjected to microwave heating at 200 °C for an hour. BF-TEM images show porous Pt nanotubes with larger Pt crystallites of size ~5 nm dispersed all along the nanotubes (Fig. S4d and e, ESI†) and the corresponding XRD pattern shows crystalline Pt phase (Fig. S4f, ESI†). We believe that the zinc platinate phase is stable under acidic conditions of pH < 7. At neutral pH, it decomposes to Pt. The rate of hydrolysis of precursor salts and the dissolution of ZnO depends on temperature. To see the effect of temperature on the reaction mechanism, the microwave reaction is carried out at 100 °C. BF-TEM images of the white product obtained show that the nanorods are still intact but have a rough surface due to the partial etching in the acidic medium (Fig. S5, ESI†). The absence of porous nanotubes indicates that the reaction kinetics are not conducive at low temperatures.

Based on the above observations, a possible mechanism pathway for the formation of pZPO-NTs is proposed in accordance with the sacrificial template accelerated hydrolysis (STAH) mechanism proposed earlier.[60] This mechanism is also invoked to explain the formation of porous VO_2 nanotubes[65] or porous PdO nanotubes.[67] But in all these structures, the template does not participate in the formation of the final product. In our case, we believe that the weak reducibility of water prevents the reduction of the platinum precursor, thereby maintaining its +4 valence state. Unlike VO_2 and PdO, platinum oxide formation is not feasible under these reaction conditions. Alternatively, the metastable zinc platinate formation is favorable due to the thermal and kinetic effects of the microwave synthesis, which help in the faster diffusion of Zn^{2+} ions. The reaction pathway for the formation of porous zinc platinate nanotubes is shown in the ESI† (Scheme S1). The dissolution of ZnO accelerates the hydrolysis of Pt complex ions, which in turn promotes the formation of zinc platinate in the proximity of the ZnO surface, preserving the morphology of the nanorods, aided by the superior kinetics provided by microwave reaction. The reaction proceeds if the pH of the medium is acidic enough to dissolve the ZnO. With the increase in the concentration of Zn^{2+} ions in solution due to the dissolution of $ZnCl_2$, the pH of the medium increases, which arrests the STAH mechanism.[65]

The TEM studies of pZPO-NTs reveal that the zinc platinate phase undergoes reduction upon exposure to the electron beam and this process is very rapid and occurs within a few minutes upon exposure. Under a reduced dose of the incident electron beam, this transformation is captured as shown in Fig. S6 (ESI†). During this reduction, the particle size coarsens to ~3 nm and the tube shrinks in diameter by ~10 nm. Earlier reports have shown that zinc platinate nanoparticles are stable under the electron beam.[63,95] The instability observed in our case may be due to the surface stresses generated in extremely small crystallite sizes of 1–2 nm, which may accommodate at maximum 2-unit cells of the inverse spinel zinc platinate (lattice parameter ~8.5 Å). Following this observation, a controlled reduction step is designed using sodium borohydride as the reducing agent at room temperature. An aqueous solution of sodium borohydride (10 mg mL^{-1}) is added dropwise to a dilute dispersion of pZPO-NTs in water. The color of the solution changes gradually from yellow to black over the duration of 20 minutes resulting in the formation of porous platinum tubes. The SEM image from this sample shows

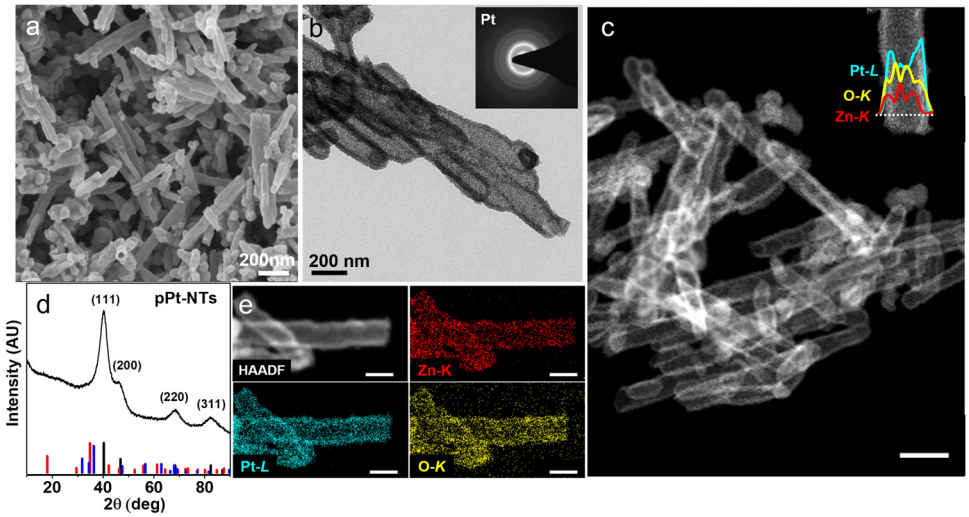

Fig. 3 (a) SEM micrograph of the as-synthesized porous Pt nanotubes (pPt-NTs). (b) Low magnification BF-TEM and (c) HAADF-STEM images respectively of pPt-NTs confirming the hollow interior and porous nature of the nanotubes. The inset shows the STEM-EDS line scan taken along the diameter of a nanotube for Zn-*K*, Pt-*L*, and O-*K* lines. (d) XRD pattern from as-synthesized pPt-NTs, which can be matched to ICDD file 00-001-1190 for the standard Pt phase (black line). The standard Zn_2PtO_4 phase (ICDD 00-023-1499) and standard ZnO phase (ICDD-00-036-1451) are shown in red and blue, respectively. (e) STEM-EDS elemental mapping for Zn-*K*, Pt-*L* and O-*K*, respectively, taken from a single nanotube showing the distribution of the elements. Scale bar in (c) is 200 nm and in (e) is 200 nm.

smooth porous shells with hollow cores (Fig. 3a). XRD data for the freshly prepared porous Pt shows only sharp FCC peaks, which can be indexed to (111), (200), (220), and (311) of a fully formed Pt phase (Fig. 3d). The peaks due to zinc platinate or ZnO are not observed. BF-TEM and STEM-HAADF studies show that the porosity is uniform with the formation of tiny ~3 nm crystallites of Pt (Fig. 3b and c). The STEM-EDS elemental maps (Fig. 3d) and line scan (inset of Fig. 3c) from a single nanotube show the presence of Pt, Zn and O. XPS studies of the porous Pt nanotubes show a pure metallic Pt phase (Fig. S7, ESI†). The binding energy values are 71 eV and 74.3 eV, respectively, for the Pt4f doublet, which matches with the zero oxidation state of Pt.[96] We also see a substantial amount of Zn 2p signal in this sample indicating that zinc in the form of $Zn^{2+}$is still present at 1020.9 eV. The shift of nearly 1 eV in the binding energy of Zn^{2+} as compared to that of the zinc platinate phase is observed, which may be due to the change in the coordination environment.[97] A small peak at the higher binding energy at 1022.9 eV is assigned to $Zn(OH)_2$.[98] Composition analysis from XPS shows the relative atomic ratio of Pt : Zn as 1 : 0.7. (Relative atomic ratios for Pt and Zn are listed in Table S1, ESI†).

The highly porous nature of pZPO-NTs and pPt-NTs suggests enhanced specific surface area; estimation of the surface area is useful in predicting the catalytic efficiency. The specific surface area and porosity are evaluated from nitrogen sorption isotherms at 77 K (Fig. S8a, ESI†). The samples show type Iva adsorption isotherms. The capillary condensation and desorption hysteresis at higher P/P_0 values (0.4–1) confirm the presence of mesopores.[99] The asymptotic rise in the adsorption curve at $P/P_0 > 0.9$ indicates the presence of macropores (size >50 nm), which is evident from the hollow nature of the nanotubes.[100] The Barrett–Joyner–Halenda (BJH) pore size distribution shows a maximum pore diameter of 5.2 nm for pZPO-NTs (Fig. S8b, ESI†) and for pPt-NTs, the value is 6 nm (Fig. S8c, ESI†). Along with this, both the materials show a macropore size of ~44 nm displaying the hierarchically porous nature. The Brunauer–Emmett–Teller (BET) surface area measured from the multipoint analysis is 54 $m^2\ g^{-1}$ for pZPO-NTs and 46 $m^2\ g^{-1}$ for pPt-NTs. Thus, both the samples display superior 1D hollow mesoporous structures of hierarchical porosity along with high surface area, which is beneficial in catalysis and sensing applications.

The electrocatalytic activity of porous nanotubes is evaluated by studying the methanol oxidation reaction (MOR) in an alkaline medium using cyclic voltammetry (CV). The MOR curves for pZPO-NTs are shown in Fig. 4a. The peak current for MOR increases with successive scans and peak potential shifts to higher values. The variation of MOR peak current and MOR peak potential with the number of CV cycles is shown in Fig. 4b for 700 cycles. For the first 100 cyclic scans, the peak MOR potential is 0.8 V *vs.* RHE but it increases linearly with the number of cycles and reaches a value of 1.01 V *vs.* RHE at the end of 200 cycles. For the next 460 cycles, the rate of increase in potential is not drastic and the potential value settles at 1.06 V *vs.* RHE at the end of a total of 700 cycles. The MOR peak current also shows similar behavior. The current increases in a steep manner for the initial 200 cycles and then remains constant for the rest of the cycles.

The BF-TEM images of the sample electrode after electrocatalytic studies show the formation of dendritic nanoparticles of Pt after 50 cycles of MOR (Fig. 4d–f). After 700 cycles, dendritic nanoparticle clusters of almost uniform size are observed (Fig. 4g). XPS studies show an intense metallic Pt 4f doublet at binding energy values 71.2 eV and 74.6 eV, respectively, and significant amounts of PtO_2 at 74.9 eV and 78 eV, respectively (Fig. 4i). The composition ratio of Pt : Zn from XPS is 1 : 0.2 (Table S1 in the ESI†), which suggests the dissolution

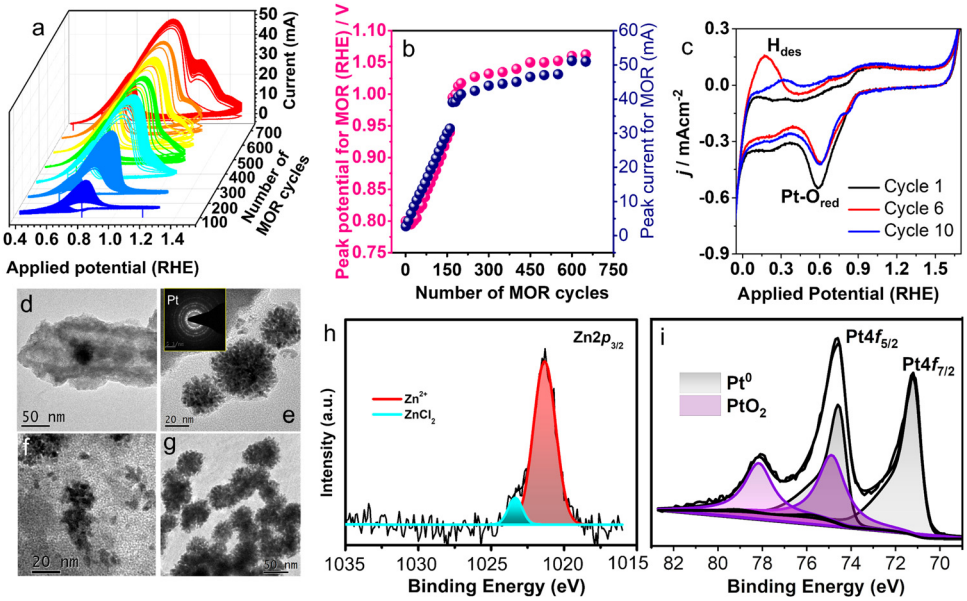

Fig. 4 (a) Electrocatalytic MOR activity with pZPO-NTs carried out at a scan rate of 40 mV S^{-1} in electrolyte solution of 0.5 M KOH +1 M CH_3OH shows the variation in the catalytic behaviour with successive scanning up to 700 cycles. (b) MOR peak potential and peak current variation with number of cycles. (c) Variation in the hydrogen desorption peak shape with a successive number of cycles in 0.5 M KOH solution at a scan rate of 40 mV S^{-1}. (d–f) Formation of dendritic nanoparticles of Pt in pZPO-NTs after performing 50 cycles of MOR. (g) Morphology of the pZPO-NTs catalyst taken post electrocatalysis studies after 700 cycles of MOR. (h) and (i) XPS analysis performed post electrocatalysis of pZPO-NTs showing the Pt^0 state as a prominent phase along with PtO_2 phase.

of the ZnO phase during the MOR. The potential cycles between −0.1 V to 1.7 V (RHE) in argon gas purged 0.5 M KOH (Fig. 4c) solution show that there is a substantial Pt–O reduction current around 0.6 V during the reverse scan, though the Pt–O formation current is not substantial in the forward scan (between 0.4 V and 1.6 V) indicating that more Pt–O is getting reduced than is formed. Also, the shape of the hydrogen desorption peak in the potential region between 0 V to 0.4 V is found to change and the position of the peak shifts to higher potential values with successive cycles. This may suggest that initially single atoms or clusters of Pt form, which have weak binding energy with hydrogen and eventually as the clusters grow the hydrogen binds strongly to these clusters thereby making the desorption difficult. It has been observed during metal electrodeposition that the nucleation and growth of the deposited metal result in dendritic structures.[101,102] The computationally predicted Pourbaix diagram, which predicts the electrochemical stability of metastable phases, shows that Zn_2PtO_4 transforms into Pt and $HZnO_2^-$ ions under the potential ranges and pH conditions used.[87]

Preliminary cyclic voltammetry experiments showed that Zn can leach out systematically from the porous nanotubes in the presence of high alkalinity, thereby enhancing the current. An *ex situ* dissolution procedure for the ZnO phase is performed by dispersing the as-synthesized porous Pt nanotubes in a dilute HCl/H_2O solution of pH 3 for an hour. This sample is labeled as pPt-NTs-E. The porous morphology of the nanotubes is intact after the acid treatment as well as the nano Pt crystallite size. However, we have observed that some of the nanotubes are opening into sheets (Fig. S9 and inset of Fig. S9b, ESI†). This is due to the thinning of the Pt shells during the etching of ZnO, similar to observations we have made in PdO nanotubes, confirming that the pH of the medium has a significant effect on the integrity of the tube morphology.[67] The MOR activity for pPt-NTs-E and pPt-NTs is compared with that of the commercial Pt/C sample (Fig. 5). Both the samples show good methanol oxidation activity compared to Pt/C with a similar onset MOR potential of ~0.5 V (RHE) (Fig. 5a). The acid-treated sample shows a 75% increase in mass activity (35 mA mg^{-1}) and a 30% increase in specific activity (0.5 mA cm^{-2}) compared to pPt-NTs (Fig. 5a and d). The MOR peak potential is observed at 1.01 V and 1.02 V for the treated and as-prepared nanotubes, respectively, which are ~170 mV less than that for commercial Pt/C (1.17 V) demonstrating the efficiency of porous nanotubes in catalyzing the methanol oxidation at lower overpotentials (Fig. 5f). Chronoamperometric studies (Fig. 5c) show that the samples are stable and no significant changes in the oxidation current are observed in the measured period of 4000 seconds. The ratio of oxidation currents in the forward and backward direction of the MOR curve, I_f/I_b (which gives an indication of efficient oxidation of unwanted CO species) >1.2 for the porous samples compared to commercial Pt/C (I_f/I_b = 1.0). Removal of Zn in acid-treated porous Pt nanotubes slightly reduces the I_f/I_b (Fig. 5f). Electrochemical Impedance Spectroscopy (EIS) studies were performed at the onset potential in alkaline conditions (0.1 M KOH) (Fig. S13, ESI†). The solution resistance (R_s) for pPt-NTs was found to be comparable to commercial Pt/C, indicating that pPt-NTs also possess equivalent surface charge. The charge-transfer resistance (R_{ct}) of both the materials, as depicted from the semi-circle, is also comparable suggesting that

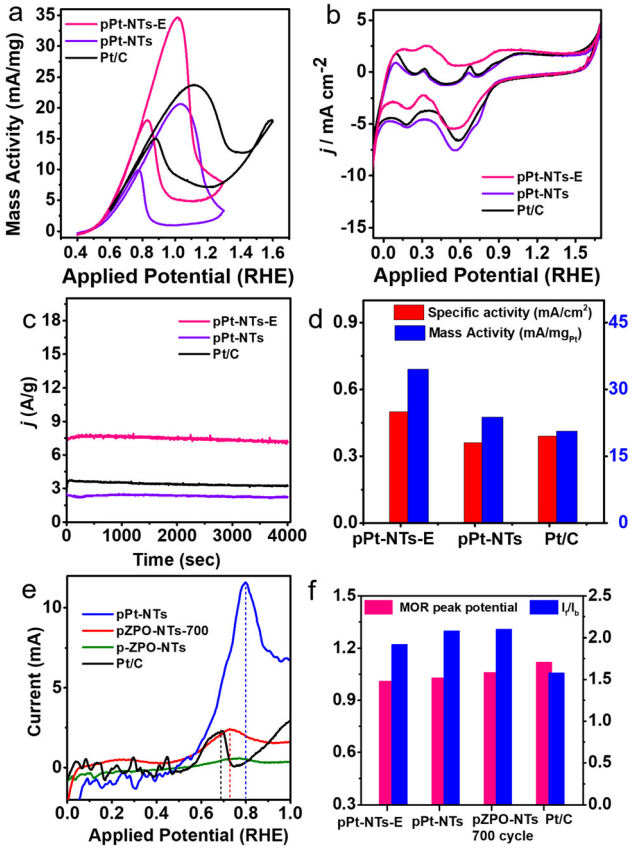

Fig. 5 CV scans for pPt-NTs-E, pPt-NTs and Pt/C (a) for the mass activity towards MOR in 0.5 M KOH + 1 M CH_3OH solution (b) for ECSA measurements in Ar purged 0.5 M KOH solution. (c) Chronoamperometry studies at 1.0 V (*vs.* RHE) in Ar purged 0.5 M KOH solution. (d) Specific activity and mass activity comparison. (e) First half of the CV cycle of CO-stripping studies performed on freshly prepared pPt-NTs, pZPO-NTs after 700 cycles of MOR, freshly prepared pZPO-NTs and commercial Pt/C at a scan rate of 10 mV S^{-1}. (f) Comparison of MOR peak potential and I_f/I_b ratio. The porous samples show better catalytic activity with less overpotentials for the MOR with higher I_f/I_b values compared to commercial Pt/C.

both the samples have comparable electrical conductivities. However, the removal of ZnO from porous Pt nanotubes has significant benefits in enhancing the current. This may be due to the removal of the resistive paths provided by the highly insulating amorphous ZnO in between the current-carrying Pt nanoparticles.[103]

To understand the surface properties, CO-stripping voltammetry is performed on fresh pZPO-NTs, pZPO-NTs after 700 cycles of MOR, fresh pPt-NTs, and commercial Pt/C. The electrolyte (0.5 M KOH) is saturated in CO by continuously bubbling the gas through the solution for 15 min at a potential where the hydrogen desorption from the anode is favored (0.1 V *vs.* RHE). This is to ensure that enough active sites are available for CO to adsorb to form a monolayer on the catalyst surface. The potential sweep is started from this potential at a scan rate of 10 mV S^{-1}. Only the first half of the full CV cycle is displayed in Fig. 5e. The CO-stripping potential for pPt-NTs, pZPO-NTs-700 (after 700 cycles of MOR), pZPO-NTs, and commercial Pt/C with respect to RHE is 0.8 V, 0.73 V, 0.75 V, and 0.7 V, respectively. The porous nanotubes show slightly higher overpotentials for CO stripping albeit their activities are much better than commercial Pt/C (Fig. 5d) due to the available active sites.

We believe that the high surface area and hierarchically porous nature are responsible for improving the MOR activity. TEM studies of porous Pt nanotubes after electrocatalysis show that connected networks of highly crystalline Pt ligaments form maintaining the hollow tubular core (Fig. S10, ESI†). The combined structure of crystalline ligaments and hollow channels is beneficial in enhancing the efficiency of methanol oxidation. There is still a trace amount of Zinc present in the +2 oxidation state at BE value 1021.1 eV as revealed by the XPS studies (Fig. S10c and d, ESI†). The Pt 4f doublet shows purely metallic Pt^0 species at BE 71.2 eV and 74.6 eV, respectively. The surface of the sample also has PtO_2 at BE values of 74.8 eV and 78 eV, respectively. The composition ratio of Pt : Zn in this sample is 1 : 0.1. As the oxidized species of an element is more hydrophilic in nature, it helps in the removal of CO by the beneficial Langmuir–Hinshelwood bi-functional mechanism when the hydroxyl group bonded to the higher oxidation state Pt can effectively oxidize the CO attached to the neighboring metallic Pt.[104] The ORR performance (details are in ESI†) of pPt-NTs is investigated in oxygen saturated 0.1 M KOH medium at different rotation rates of the glassy carbon electrode. The ORR activity of pPt-NTs is comparable to commercial Pt/C (Fig. S11 and S12, ESI†). The pPt-NTs follow a direct pathway of electron reduction of O_2 to H_2O through a 4-electron transfer process without involving the formation of reaction intermediates. These results are in accordance with the earlier observations, thus confirming the enhanced electron and mass transfer facilitated by mesoporous nature.[105]

The sensing studies are performed on pZPO-NTs in an interdigitated electrode configuration (see ESI,† for more details). Initially, the sensor is exposed to different concentrations of SO_2 at room temperature and the recorded dynamic response shows n-type behavior in the presence of SO_2 (Fig. 6a). It can precisely detect in the range of 0.3 ppm to 3 ppm with response magnitudes varying from 8.9% to 85.27%, respectively, and demonstrates a sensitivity of 31%/ppm towards SO_2 at room temperature with complete recovery on the release of SO_2 gas (Fig. 6b). The response in this range is found to be linear with a correlation coefficient of 0.98. The response and recovery are swift within 10 s to 0.3 ppm SO_2 (Fig. 6c). However, it took 128 s to recover when 3 ppm SO_2 was released, which may be attributed to the highly porous nature of these nanotubes. The gas diffuses through the pores and hence takes longer to desorb. Nevertheless, it could be detected rapidly and reached a near plateau within 30 s for all the concentrations. The selectivity of the sensor is examined by purging different oxidizing and reducing gases such as H_2, NH_3, acetone, NO_2, H_2S, and ethanol along with SO_2. The sensor exhibits specific detection of SO_2 at room temperature (Fig. 6d). To investigate the reproducibility and reliability of the sensor, it is subjected to five consecutive cycles of 1 ppm SO_2 (Fig. S16a, ESI†).

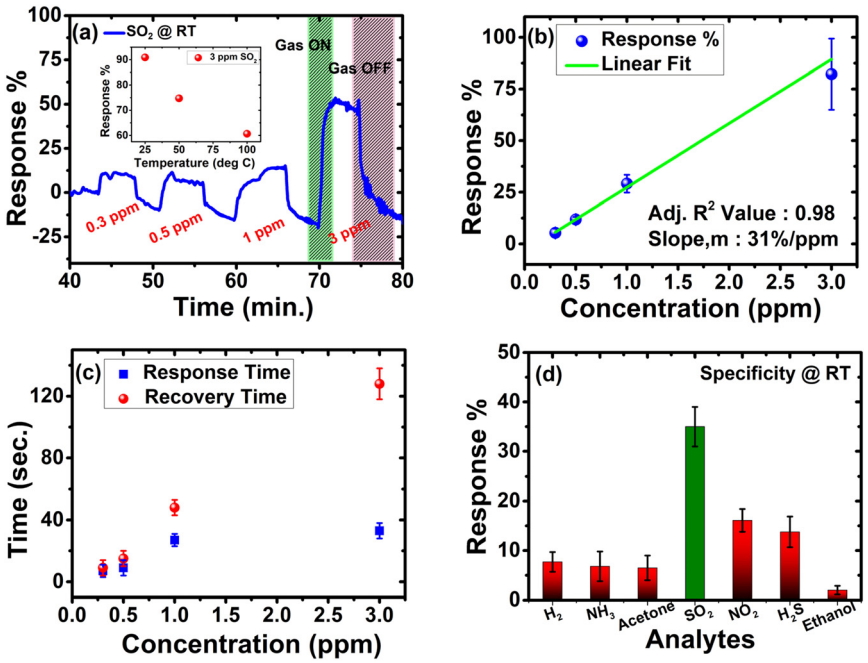

Fig. 6 (a) Dynamic response plot for different concentrations of SO_2 at room temperature; the inset shows the temperature dependent behaviour of SO_2 towards pZPO-NTs, (b) linear fitting of the response *vs* concentration plot, (c) response time and recovery time for different H_2S concentrations and (d) specificity towards different gases at 1 ppm at room temperature.

Although the outcome is repeatable, a baseline drift, common in chemiresistive gas sensors, is observed, which is possibly due to the variations in ambient humidity levels since the sensor is operated at room temperature. The memory effect is determined experimentally by carrying out the concentration sweep from low to high and vice-versa, thereby computing the hysteresis error (Fig. S16b and c, ESI†). The hysteresis error is ± 3.55, which is indicative of an insignificant memory effect on the sensor. To investigate the inter-device variations, four different devices are tested for all concentrations of SO_2 and the variations are well within the tolerance limit of the sensor as seen in Fig. 6b. The sensor performance was compared with the existing works on the detection of SO_2 in the literature and is summarised in Table S3 (ESI†). Among all, pZPO-NTs displayed swift and highly sensitive detection at room temperature. They could resolve the signal down to 0.3 ppm, which seems to be one of the lowest limits of detection (LOD) claimed among the reported ones at room temperature. The underlying mechanism behind the sensing can be explained by the well-established space charge theory in metal oxides[57] and is discussed in the ESI.† Furthermore, the exemplary room temperature sensing can be ascribed to the mesoporous nature of these nanotubes, which adds to the enhancement of the surface area (54 m^2 g^{-1}) and hence the sensitivity.

4 Conclusions

In summary, our study shows the template-based synthesis of mesoporous zinc platinate and platinum nanotubes using ZnO nanorods as sacrificial templates. Unlike the other similar synthesis of mesoporous materials, in our case ZnO actively participates in the product formation and aided by the superior kinetics of microwave reaction, we can synthesize mesoporous zinc platinate nanotubes. Zinc platinate nanotubes form only under the superior reaction kinetics provided by the microwave reaction conditions. By suitably designing control experiments, we have proposed a reaction pathway that follows sacrificial template-assisted hydrolysis (STAH). A simple chemical reduction using $NaBH_4$ can reduce the zinc platinate nanotubes into platinum nanotubes maintaining the morphology and porosity. Through N_2 adsorption–desorption isotherms, we have confirmed the formation of a hollow mesoporous 1D morphology of the nanotubes with exceptionally high specific surface area with a pore diameter of $\sim$5 nm and 6 nm for zinc platinate and platinum nanotubes, respectively. Electrocatalytic methanol oxidation studies are performed on these porous nanotubes, and they are found to have excellent activity as compared to commercial Pt catalysts. The ORR ability of porous Pt nanotubes is comparable to commercial Pt catalysts and the mechanism follows direct 4 electron transfer with the least amount of intermediate H_2O_2 formation. Furthermore, we could observe highly sensitive (31%/ppm) detection of mesoporous zinc platinate nanotubes towards SO_2 at room temperature with swift recovery at room temperature without an external stimulus. This could be an ideal candidate for monitoring SO_2 emissions in industry.

Conflicts of interest

There are no conflicts to declare.

Acknowledgements

The authors acknowledge the Advanced Facilities for Microscopy and Microanalysis (AFMM), Micro and Nano Characterization Facility (MNCF) and Materials Research Centre (MRC) at IISc for providing the materials characterization facilities. SS and NR acknowledge the funding provided by Nanomission, SERB and DST, Government of India. N. S. and N. B. thank the facilities provided by the Centre for Nanoscience and Engineering (CeNSE) and National Nano Fabrication Facility (NNFC) at IISc. N. S. and N. B. acknowledge the financial support from MHRD, MeitY and DST, Government of India. A. M. and A. H. acknowledge the Advanced Material Research Centre (AMRC) at IIT Mandi for providing the facilities. Also, MHRD and DST, Government of India for funding. We thank Prof. Ramananda Chakrabarti, CEaS, IISc for providing the ICP-MS facility.

References

1 W. Li, J. Liu and D. Zhao, *Nat. Rev. Mater.*, 2016, **1**, 16023.
2 C. Li, Q. Li, Y. V. Kaneti, D. Hou, Y. Yamauchi and Y. Mai, *Chem. Soc. Rev.*, 2020, **49**, 4681–4736.
3 S. S. Park and C. S. Ha, *Adv. Funct. Mater.*, 2018, **28**, 1–29.
4 J. Wang, Q. Ma, Y. Wang, Z. Li, Z. Li and Q. Yuan, *Chem. Soc. Rev.*, 2018, **47**, 8766–8803.
5 B. R. Thompson, T. S. Horozov, S. D. Stoyanov and V. N. Paunov, *J. Mater. Chem. A*, 2019, **7**, 8030–8049.
6 Z. Qi and J. Weissmüller, *ACS Nano*, 2013, **7**, 5948–5954.
7 K. Miszta, J. De Graaf, G. Bertoni, D. Dorfs, R. Brescia, S. Marras, L. Ceseracciu, R. Cingolani, R. Van Roij, M. Dijkstra and L. Manna, *Nat. Mater.*, 2011, **10**, 872–876.
8 T. X. T. Sayle, K. Kgatwane, P. E. Ngoepe and D. C. Sayle, *J. Mater. Chem. A*, 2016, **4**, 6456–6464.
9 O. V. Shulga, K. Jefferson, A. R. Khan, V. T. D'Souza, J. Liu, A. V. Demchenko and K. J. Stine, *Chem. Mater.*, 2007, **19**, 3902–3911.
10 H. Qiu, L. Lu, X. Huang, Z. Zhang and Y. Qu, *Bioresour. Technol.*, 2010, **101**, 9415–9420.
11 J. H. Han, H. Boo, S. Park and T. D. Chung, *Electrochim. Acta*, 2006, **52**, 1788–1791.
12 P. Daggumati, Z. Matharu and E. Seker, *Anal. Chem.*, 2015, **87**, 8149–8156.
13 R. Raccis, A. Nikoubashman, M. Retsch, U. Jonas, K. Koynov, H. J. Butt, C. N. Likos and G. Fytas, *ACS Nano*, 2011, **5**, 4607–4616.
14 B. Szczęśniak, J. Choma and M. Jaroniec, *Chem. Commun.*, 2020, **56**, 7836–7848.
15 B. Viswanath, S. Patra, N. Munichandraiah and N. Ravishankar, *Langmuir*, 2009, **25**, 3115–3121.
16 Y. Li, B. P. Bastakoti, V. Malgras, C. Li, J. Tang, J. H. Kim and Y. Yamauchi, *Angew. Chem.*, 2015, **127**, 11225–11229.
17 C. Mahr, P. Kundu, A. Lackmann, D. Zanaga, K. Thiel, M. Schowalter, M. Schwan, S. Bals, A. Wittstock and A. Rosenauer, *J. Catal.*, 2017, **352**, 52–58.
18 Z. Lu, C. Li, J. Han, F. Zhang, P. Liu, H. Wang, Z. Wang, C. Cheng, L. Chen, A. Hirata, T. Fujita, J. Erlebacher and M. Chen, *Nat. Commun.*, 2018, **9**, 1–7.
19 L. Wang and Y. Yamauchi, *J. Am. Chem. Soc.*, 2013, **135**, 16762–16765.
20 A. Kloke, F. Von Stetten, R. Zengerle and S. Kerzenmacher, *Adv. Mater.*, 2011, **23**, 4976–5008.
21 S. Rudi, L. Gan, C. Cui, M. Gliech and P. Strasser, *J. Electrochem. Soc.*, 2015, **162**, F403–F409.
22 V. Malgras, H. Ataee-Esfahani, H. Wang, B. Jiang, C. Li, K. C. W. Wu, J. H. Kim and Y. Yamauchi, *Adv. Mater.*, 2016, **28**, 993–1010.
23 S. Yang and X. Luo, *Nanoscale*, 2014, **6**, 4438–4457.
24 A. Kloke, F. Von Stetten, R. Zengerle and S. Kerzenmacher, *Adv. Mater.*, 2011, **23**, 4976–5008.
25 J. Zhang and C. M. Li, *Chem. Soc. Rev.*, 2012, **41**, 7016–7031.
26 M. Pérez-Page, E. Yu, J. Li, M. Rahman, D. M. Dryden, R. Vidu and P. Stroeve, *Adv. Colloid Interface Sci.*, 2016, **234**, 51–79.
27 P. K. Chen, N. C. Lai, C. H. Ho, Y. W. Hu, J. F. Lee and C. M. Yang, *Chem. Mater.*, 2013, **25**, 4269–4277.
28 L. Zu, W. Zhang, L. Qu, L. Liu, W. Li, A. Yu and D. Zhao, *Adv. Energy Mater.*, 2020, **10**, 1–14.
29 X. Xia, Y. Wang, A. Ruditskiy and Y. Xia, *Adv. Mater.*, 2013, **25**, 6313–6333.
30 J. Chen, J. M. McLellan, A. Siekkinen, Y. Xiong, Z. Y. Li and Y. Xia, *J. Am. Chem. Soc.*, 2006, **128**, 14776–14777.
31 E. Zhang, F. Ma, J. Liu, J. Sun, W. Chen, H. Rong, X. Zhu, J. Liu, M. Xu, Z. Zhuang, S. Chen, Z. Wen and J. Zhang, *Nanoscale*, 2018, **10**, 21703–21711.
32 K. Cai, Z. Lv, K. Chen, L. Huang, J. Wang, F. Shao, Y. Wang and H. Han, *Chem. Commun.*, 2013, **49**, 6024.
33 L. Hai-Wei, L. Shuo, G. Jun-Yan, W. Shang-Bing, W. Lei and Y. Shu-Hong, *Adv. Mater.*, 2009, **21**, 1850–1854.
34 K. D. Gilroy, P. Farzinpour, A. Sundar, R. A. Hughes and S. Neretina, *Chem. Mater.*, 2014, **26**, 3340–3347.
35 Y. Sun, H. Yang, X. Yu, H. Meng and X. Xu, *RSC Adv.*, 2015, **5**, 70387–70394.
36 Y. W. Lee, M. A. Lim, S. W. Kang, I. Park and S. W. Han, *Chem. Commun.*, 2011, **47**, 6299.
37 B. S. Choi, Y. W. Lee, S. W. Kang, J. W. Hong, J. Kim, I. Park and S. W. Han, *ACS Nano*, 2012, **6**, 5659–5667.
38 Z. Wang, D. Luan, C. M. Li, F. Su, S. Madhavi, F. Y. C. Boey and X. W. Lou, *J. Am. Chem. Soc.*, 2010, **132**, 16271–16277.
39 F. Hong, S. Sun, H. You, S. Yang, J. Fang, S. Guo, Z. Yang, B. Ding and X. Song, *Crystal Growth Design*, 2011, **11**, 3694–3697.
40 X. Xia, Y. Wang, A. Ruditskiy and Y. Xia, *Adv. Mater.*, 2013, **25**, 6313–6333.
41 C. Cui, L. Gan, M. Heggen, S. Rudi and P. Strasser, *Nat. Mater.*, 2013, **12**, 765–771.
42 B. D. McNicol and R. T. Short, *J. Electroanal. Chem.*, 1977, **81**, 249–260.
43 W. Sugimoto, K. Aoyama, T. Kawaguchi, Y. Murakami and Y. Takasu, *J. Electroanal. Chem.*, 2005, **576**, 215–221.
44 P. J. Kulesza, I. S. Pieta, I. A. Rutkowska, A. Wadas, D. Marks, K. Klak, L. Stobinski and J. A. Cox, *Electrochim. Acta*, 2013, **110**, 474–483.

45 M. T. Y. Paul and B. D. Gates, *Sci. Rep.*, 2019, **9**, 1–9.
46 B. Fu, M. Dang, J. Tao, Y. Li and Y. Tang, *J. Colloid Interface Sci.*, 2020, **570**, 197–204.
47 P. Díez, E. Lucena-Sánchez, A. Escudero, A. Llopis-Lorente, R. Villalonga and R. Martínez-Máñez, *ACS Nano*, 2021, **15**, 4467–4480.
48 A. Rednyk, V. Johánek, I. Khalakhan, M. Dubau, M. Vorokhta and V. Matolín, *Int. J. Hydrogen Energy*, 2016, **41**, 265–275.
49 N. R. Manwar, A. A. Chilkalwar, K. K. Nanda, Y. S. Chaudhary, J. Subrt, S. S. Rayalu and N. K. Labhsetwar, *ACS Sustainable Chem. Eng.*, 2016, **4**, 2323–2332.
50 N. Bingwa, M. J. Ndolomingo, J. H. Noh, N. Antonels, E. Carleschi, B. P. Doyle, M. Haumann and R. Meijboom, *Mol. Catal.*, 2020, **492**, 110978.
51 P. K. Basu, S. Kallatt, E. A. Anumol and N. Bhat, *J. Appl. Phys.*, 2015, **117**, 224501.
52 R. M. Mohamed, A. A. Ismail, M. W. Kadi, A. S. Alresheedi and I. A. Mkhalid, *ACS Omega*, 2021, **6**, 6438–6447.
53 L. Zheng, J. Xie, X. Liu, C. Yang, W. Zheng and J. Zhang, *ACS Appl. Mater. Interfaces*, 2020, **12**, 46267–46276.
54 G. S. Attard, P. N. Bartlett, N. R. B. Coleman, J. M. Elliott, J. R. Owen and J. H. Wang, *Science (1979)*, 1997, **278**, 838–840.
55 Y. Li, Y. Liu, J. Li, D. Xiong, X. Chen, M. Liu, Z. Zhong, V. Malgras and Y. Bando, *Mater. Horiz.*, 2020, **7**, 489–494.
56 H. Ji, W. Zeng and Y. Li, *Nanoscale*, 2019, **11**, 22664–22684.
57 K. Wetchakun, T. Samerjai, N. Tamaekong, C. Liewhiran, C. Siriwong, V. Kruefu, A. Wisitsoraat, A. Tuantranont and S. Phanichphant, *Sens. Actuators, B*, 2011, **160**, 580–591.
58 C. Mora, D. Spirandelli, E. C. Franklin, J. Lynham, M. B. Kantar, W. Miles, C. Z. Smith, K. Freel, J. Moy, L. V. Louis, E. W. Barba, K. Bettinger, A. G. Frazier, J. F. Colburn IX, N. Hanasaki, E. Hawkins, Y. Hirabayashi, W. Knorr, C. M. Little, K. Emanuel, J. Sheffield, J. A. Patz and C. L. Hunter, *Nat. Climate Change*, 2018, **8**, 1062–1071.
59 Y. Liu, J. Parisi, X. Sun and Y. Lei, *J. Mater. Chem. A*, 2014, **2**, 9919–9943.
60 J. Liu, Y. Li, H. Fan, Z. Zhu, J. Jiang, R. Ding, Y. Hu and X. Huang, *Chem. Mater.*, 2010, **22**, 212–217.
61 A. Kolodziejczak-Radzimska and T. Jesionowski, *Materials*, 2014, **7**, 2833–2881.
62 R. Jiang, Y. Da, X. Han, Y. Chen, Y. Deng and W. Hu, *Cell Rep. Phys. Sci.*, 2021, **2**, 100302.
63 P. Kjellin and A. E. C. Palmqvist, *J. Mater. Sci.*, 2008, **43**, 7250–7253.
64 O. Muller and R. Roy, *Mater. Res. Bull.*, 1969, **4**, 39–43.
65 X. Li and R. E. Schaak, *Chem. Mater.*, 2019, **31**, 2088–2096.
66 Y. W. Lee, M. A. Lim, S. W. Kang, I. Park and S. W. Han, *Chem. Commun.*, 2011, **47**, 6299.
67 S. Kundu and N. Ravishankar, *Nanoscale*, 2016, **8**, 1462–1469.
68 C. Pacholski, A. Kornowski and H. Weller, *Angew. Chem., Int. Ed.*, 2002, **41**, 1188–1191.
69 A. Leelavathi, G. Madras and N. Ravishankar, *J. Am. Chem. Soc.*, 2014, **136**, 14445–14455.
70 H. J. Fan, M. Knez, R. Scholz, K. Nielsch, E. Pippel, D. Hesse, M. Zacharias and U. Gösele, *Nat. Mater.*, 2006, **5**, 627–631.
71 R. Rémiás, Á. Kukovecz, M. Darányi, G. Kozma, S. Varga, Z. Kónya and I. Kiricsi, *Eur. J. Inorg. Chem.*, 2009, 3622–3627.
72 J. Paiz, J. Fitch, E. Peterson, T. Hough, W. Barnard and A. Datye, *Cryst. Res. Technol.*, 2014, **49**, 699–707.
73 I. Hölken, G. Neubüser, V. Postica, L. Bumke, O. Lupan, M. Baum, Y. K. Mishra, L. Kienle and R. Adelung, *ACS Appl. Mater. Interfaces*, 2016, **8**, 20491–20498.
74 X. Li and R. E. Schaak, *Chem. Mater.*, 2019, **31**, 2088–2096.
75 Y. V. Kaneti, N. L. Wulan Septiani, I. Saptiama, X. Jiang, B. Yuliarto, M. J. A. Shiddiky, N. Fukumitsu, Y. M. Kang, D. Golberg and Y. Yamauchi, *J. Mater. Chem. A*, 2019, **7**, 3415–3425.
76 S. Tripathi, R. Bose, A. Roy, S. Nair and N. Ravishankar, *ACS Appl. Mater. Interfaces*, 2015, **7**, 26430–26436.
77 A. Leelavathi, G. Madras and N. Ravishankar, *Phys. Chem. Chem. Phys.*, 2013, **15**, 10795.
78 J. E. Drawdy, G. B. Hoflund, S. D. Gardner, E. Yngvadottir and D. R. Schryer, *Surf. Interface Anal.*, 1990, **16**, 369–374.
79 S. D. Jackson, J. Willis, G. D. McLellan, G. Webb, M. B. T. Keegan, R. B. Moyes, S. Simpson, P. B. Wells and R. Whyman, *J. Catal.*, 1993, **139**, 191–206.
80 G. M. Bancroft, I. Adams, C. D. Bennewitz, J. D. Brown and W. D. Westwood, *Anal. Chem.*, 1975, **47**, 586–588.
81 Y. Ji, F. Zhang, F. Yu, J. Zhang and J. Zhang, *Catalysts*, 2018, **8**, 99.
82 C. D. Wagner, L. E. Davis, M. V. Zeller, J. A. Taylor, R. H. Raymond and L. H. Gale, *Surf. Interface Anal.*, 1981, **3**, 211–225.
83 J. Wang, Z. Wang, B. Huang, Y. Ma, Y. Liu, X. Qin, X. Zhang and Y. Dai, *ACS Appl. Mater. Interfaces*, 2012, **4**, 4024–4030.
84 S. Shetty, S. K. Sinha, R. Ahmad, A. K. Singh, G. Van Tendeloo and N. Ravishankar, *Chem. Mater.*, 2017, **29**, 9887–9891.
85 G. B. Andreozzi, V. D'Ippolito, H. Skogby, U. Hålenius and F. Bosi, *Phys. Chem. Miner.*, 2019, **46**, 343–360.
86 L. I. Granone, A. C. Ulpe, L. Robben, S. Klimke, M. Jahns, F. Renz, T. M. Gesing, T. Bredow, R. Dillert and D. W. Bahnemann, *Phys. Chem. Chem. Phys.*, 2018, **20**, 28267–28278.
87 Materials Project, mp-35647, 2014, DOI: **10.17188/1207022**.
88 X. Xing, T. Chen, R. Zhao, Z. Wang and Y. Wang, *Sens. Actuators, B*, 2018, **254**, 227–238.
89 P. Singh, A. Kumar, Deepak and D. Kaur, *J. Cryst. Grow.*, 2007, **306**, 303–310.
90 V. M. Djinovic, L. T. Mancic, G. A. Bogdanovic, P. J. Vulic, G. del Rosario, T. J. Sabo and O. B. Milosevic, *J. Mater. Res.*, 2005, **20**, 102–113.
91 E. A. Anumol, P. Kundu, P. A. Deshpande, G. Madras and N. Ravishankar, *ACS Nano*, 2011, **5**, 8049–8061.

92 D. L. Swihart and W. R. Mason, *Inorg. Chem.*, 1970, **9**, 1749–1757.
93 C. M. Davidson and R. F. Jameson, *Trans. Faraday Soc.*, 1965, **61**, 2462.
94 I. V. Znakovskaya, Y. A. Sosedova, E. M. Glebov, V. P. Grivin and V. F. Plyusnin, *Photochem. Photobiol. Sci.*, 2005, **4**, 897.
95 V. M. Djinovic, L. T. Mancic, G. A. Bogdanovic, P. J. Vulic, G. del Rosario, T. J. Sabo and O. B. Milosevic, *J. Mater. Res.*, 2005, **20**, 102–113.
96 S. D. Cameron and D. J. Dwyer, *Surf. Sci.*, 1986, **176**, L857–L862.
97 M. W. Gaultois and A. P. Grosvenor, *J. Phys. Chem. C*, 2010, **114**, 19822–19829.
98 G. Deroubaix and P. Marcus, *Surf. Interface Anal.*, 1992, **18**, 39–46.
99 M. Thommes, K. Kaneko, A. V. Neimark, J. P. Olivier, F. Rodriguez-Reinoso, J. Rouquerol and K. S. W. Sing, *Pure Appl. Chem.*, 2015, **87**, 1051–1069.
100 F. J. Sotomayor, K. A. Cychosz and M. Thommes, *Acc. Mater. Surf. Res*, 2018, **3**, 34–50.
101 D. P. Barkey, *J. Electrochem. Soc.*, 1989, **136**, 2207.
102 K. Manthiram, Y. Surendranath and A. P. Alivisatos, *J. Am. Chem. Soc.*, 2014, **136**, 7237–7240.
103 Y. Huang, Z. Shen, Y. Wu, X. Wang, S. Zhang, X. Shi and H. Zeng, *RSC Adv.*, 2016, **6**, 17867–17872.
104 A. Rednyk, A. Ostroverkh and V. Johánek, *Int. J. Hydrogen Energy*, 2017, **42**, 29254–29261.
105 C. Li, T. Sato and Y. Yamauchi, *Angew. Chem.*, 2013, **125**, 8208–8211.